

# We are IntechOpen, the world's leading publisher of Open Access books Built by scientists, for scientists

6,900

Open access books available

186,000

International authors and editors

200M

Downloads

Our authors are among the

154

Countries delivered to

TOP 1%

most cited scientists

12.2%

Contributors from top 500 universities



WEB OF SCIENCE™

Selection of our books indexed in the Book Citation Index  
in Web of Science™ Core Collection (BKCI)

Interested in publishing with us?  
Contact [book.department@intechopen.com](mailto:book.department@intechopen.com)

Numbers displayed above are based on latest data collected.  
For more information visit [www.intechopen.com](http://www.intechopen.com)



# SAR and Optical Images for Forest Biomass Estimation

Jalal Amini<sup>1</sup> and Josaphat Tetuko Sri Sumantyo<sup>2</sup>

<sup>1</sup>University of Tehran, Tehran,

<sup>2</sup>Chiba University, Chiba,

<sup>1</sup>Iran

<sup>1</sup>Japan

## 1. Introduction

Biomass, in general, includes the above-ground and below-ground living mass, such as trees, shrubs, vines, roots, and the dead mass of fine and coarse litter associated with the soil. Due to the difficulty in collecting field data of below-ground biomass, most previous researches on biomass estimation have been focused on the above-ground biomass (AGB). Different approaches have been applied for above ground biomass (AGB) estimation, where traditional techniques based on field measurement are the most accurate ways for collecting biomass data. A sufficient number of field measurements are a prerequisite for developing AGB estimation models and for evaluating its results. However, these approaches are often time consuming, labour intensive, and difficult to implement, especially in remote areas; also, they cannot provide the spatial distribution of biomass in large areas.

The advantages of remotely sensed data, such as in repetitively of data collection, a synoptic view, a digital format that allows fast processing of large quantities of data, and the high correlations between spectral bands and vegetation parameters, make it the primary source for large area AGB estimation, especially in areas of difficult access. Therefore, remote sensing-based AGB estimation has increasingly attracted scientific interest (Nelson et al., 1988; Sader et al., 1989; Franklin & Hiernaux, 1991; Steininger, 2000; Foody et al., 2003; Zheng et al., 2004; Lu, 2005). There are also other papers including (Dobson et al., 1992; Rignot et al., 1995; Rignot et al., 1994; Quinones & Hoekman, 2004) with SAR-based methods in above ground biomass estimation.

One strategy that can be used for AGB estimation is to combine synthetic aperture radar (SAR) image texture with optical images based on the classification analysis. Limitation on the used only optical data is the insensitivity of reflectance to the change in biomass and different stands. The use of the SAR data has the potential to overcome this limitation. But presence of the speckle in SAR data is also a barrier to the exploitation of image texture. Reducing the speckle would improve the discrimination among different land use types, and would make the textual classifiers more efficient in radar images. Ideally, the filters will reduce speckle without loss of information.

Many adaptive filters that preserve the radiometric and texture information have been developed for speckle reduction. Adaptive filters based upon the spatial domain are more widely used than frequency domain filters. The most frequently used adaptive filters

include Lee, Frost, Lee-Sigma and Gamma-Map. The Lee filter is based on the multiplicative speckle model, and it can use local statistics to effectively preserve edges and features (Lee, 1980). The Frost filter is also based on the multiplicative speckle model and the local statistics, and it has similar performance to the Lee filter (Frost, 1982). The Lee-Sigma filter is a conceptually simple but effective alternative to the Lee filter, and Lee-Sigma is based on the sigma probability of the Gaussian distribution of image noise (Lee, 1980). Lopes (Lopes et al., 1990) developed the Gamma-Map filter, which is adapted from the Maximum a Posterior (MAP) filter (Kuan, 1987). Lee, Frost and Lee-Sigma filters assume a Gaussian distribution for the speckle noise, whereas Gamma-Map filter assumes a Gamma distribution of speckle (Lopes et al., 1990a; Lopes et al, 1990b). Modified versions of Gamma-Map have also been proposed (Nezry et al., 1991; Baraldi & Parmiggiani, 1995). Nezry (Nezry et al., 1991) combined the ratio edge detector and the Gamma-Map filter into the refined Gamma-Map algorithm. Baraldi and Parmiggiani (1995) proposed a refined Gamma-Map filter with improved geometrical adaptively. Walessa and Datcu combined the edge detection and region growing to segment the SAR image and then applied speckle filtering within each segment under stationary conditions. Dong et al. (2001) proposed an algorithm for synthetic aperture radar speckle reduction and edge sharpening. The proposed algorithm was functions of an adaptive-mean filter. Achim et al. (2006) proposed a novel adaptive de-speckling filter using the introduced heavy-tailed Rayleigh density function and derived a maximum a posterior (MAP) estimator for the radar cross section (RCS). The authors (Sumantyo & Amini, 2008) proposed a filter based on the least square method for speckle reduction in SAR images.

In this chapter, we develop a method for the forest biomass estimation based on (Amini & Sumantyo, 2009). Both SAR and optical images are used in a multilayer perceptron neural network (MLPNN) that relates them to the forest measurements on the ground. We use a speckle noise model that proposed by the authors in 2008 (Sumantyo & Amini, 2008) for reducing the speckle noise in the SAR image. Reducing the speckle would improve the discrimination among different land use types, and would make the textual classifiers more efficient in SAR images. We investigate both quantitative and qualitative criteria in speckle reduction and texture preservation to evaluate the performance of the proposed filter on the forest biomass estimation.

In summary, the objectives of this chapter are:

1. The efficiency of the de-speckling filter on forest biomass estimation and,
2. Improved the accuracy of forest biomass estimation when using both SAR images texture and optical images in a non-linear classifier method (MLPNN).

In the rest of the chapter, we will have a survey on de-speckling filters and then we will describe a method for the forest biomass estimation and we finally give the experimental results for the study area.

## 2. De-speckling filters on SAR images

Both the radiometric and texture aspects are less efficient for area discrimination in the presence of speckle. Reducing the speckle would improve the discrimination among different land use types, and would make the usual per-pixel or textual classifiers more efficient in radar images. Ideally, this supports that the filters reduce speckle without loss of information.

In the case of homogeneous areas (e.g. agricultural areas), the filters should preserve the backscattering coefficient values (the radiometric information) and edges between the different areas. In addition for texture areas (e.g. forest), the filter should preserve the spatial variability (textual information).

Many adaptive filters that preserve the radiometric and texture information have been developed for speckle reduction. Filtering techniques generally can be grouped into multi-look processing and posterior speckle filtering techniques. Multi-look processing is applied during image formation, and this procedure averages several statistically independent looks of the same scene to reduce speckle (Porcello et al. 1976). A major disadvantage of this technique is that the resulting images suffer from a reduction of the ground resolution that is proportional to the number of looks  $N$  (Martin and Turner 1993). To overcome this disadvantage, or to further reduce speckle, many posterior speckle-filtering techniques have been developed. These techniques are based on either the spatial or the frequency domain.

The Wiener filter (Walkup and Choens, 1974) and other filters with criteria of minimum mean-square error (MMSE) are examples of filtering algorithms that are based upon the frequency domain (Li 1988). The Wavelet approaches have been used to reduce speckle in SAR images, following Mallat's (1989a, b) theoretical basis for multi-resolution analysis. Gagnon and Jouan (1997), Fukuda and Hirosawa (1998), and Simard et al. (1998) have successfully applied wavelet transformation to reduce speckle in SAR images. Gagnon and Jouan (1997) presented a Wavelet Coefficient Shrinkage (WCS) filter, which performs as well as the standard filters for low-level noise and slightly outperforms them for higher-level noise. The wavelet filter proposed by Fukuda and Hirosawa (1998) has satisfactory performance in both smoothing and edge preservation.

There are also other filters less frequently used, such as the mean filter, the median filter, the Kalman filter (Woods and Radewan 1977), the Geometric filter (Crimmins 1985), the adaptive vector linear minimum mean-squared error (LMMSE) filter (Lin and Allebach 1990), the Weighting filter (Martin and Turner 1993), the EPOS filter (Hagg and Sties 1994), the Modified K-average filter (Rao et al. 1995) and a texture-preserving filter (Aiazzi et al. 1997).

## 2.1 Fundamentals of the speckle model

An electromagnetic wave scatters from two dimensional position  $(x, y)$  on the earth surface, the physical properties of the terrain cause changes in both the phase,  $\phi(x, y)$ , and amplitude,  $A(x, y)$ , of the wave. The SAR, in fact measures the number pair  $(A \cos \phi, A \sin \phi)$  in the in-phase and quadrature channels of the receiver, weighted by the SAR PSF (point sprit function). The estimates of the local reflectivity at each pixel can also be represented by the complex number  $Ae^{i\phi}$ ; in this form, the SAR data are known as the complex image.

From the complex image, a variety of other products can be formed. For example, images of the real part  $A \cos \phi$  (the in-phase component), the imaginary part  $A \sin \phi$  (the quadrature component), the amplitude  $A$ , the phase  $\phi$ , the intensity  $I = A^2$ , or the log intensity  $\log I$ . The use of the word 'intensity' is by analogy with measurements at optical wavelengths and is synonymous with power or energy.

The real and imaginary images show some structure but appear extremely noisy, the phase image is noise-like and shows no structure, while the amplitude, intensity, and log images, though noisy, are clearly easier to interpret. The noise-like quantity characteristic of these types of images is known as *speckle*. It must be stressed that speckle is noise-like,

but it is not noise; it is a real electromagnetic measurement, which is exploited, for example, in SAR interferometry (Oliver, and Quegan, 2004). Given that the SAR is making true measurements of the earth's scattering properties, why do such effects arise?

As the wave interacts with the target, each scatterer contributes a backscattered wave with a phase and amplitude change, so the total returned modulation or the observed value at each pixel of the incident wave is

$$Ae^{i\phi} = \sum_{k=1}^N A_k e^{i\phi_k} \quad (1)$$

This summation is over the number of scatterers illustrated by the beam. The individual scattering amplitudes  $A_k$  and phases  $\phi_k$  are unobservable because the individual scatterers are on much smaller scales than the resolution of the SAR, and there are normally many such scatterers per resolution cell.

The observed intensity or power  $I = A^2$  has a negative exponential distribution (Oliver, 1991).

$$P_I(I) = \frac{1}{\sigma} \exp\left(-\frac{I}{\sigma}\right) \quad I \geq 0 \quad (2)$$

with mean value and standard deviation both equal to  $\sigma$ , so that in this case the coefficient of variation (CV) defined as the standard deviation divided by the mean is equal  $CV=1$ . From (2) we can see that  $\sigma$  corresponds to the *average intensity*.

We need to distinguish the measured value at a pixel and the parameter value  $\sigma$  ( $\sigma$  is the Radar Cross Section (RCS) or backscattering coefficient). Equation (1) indicates that the observed value at each pixel is the resultant of interfering Huygens wavelets unless a single scatterer completely dominates the return. Hence the value of  $\sigma$  is specific to each pixel; the measured value is just a sample from the distribution parameterized by  $\sigma$ .

A SAR image comprises of some variable, corresponding to local RCS, that is combined with speckle to yield the observed intensity at each pixel. The intensity is given by  $I = \sigma n$  where  $n$  is the speckle contribution.

All the reconstruction methods for  $\sigma$  that are described require estimates of the sample mean and normalized variance over the window comprising  $N_w$  pixels, defined by:

$$\bar{x} = \frac{1}{N_w} \sum_{j=1}^{N_w} x_j \quad \text{and} \quad \bar{V}_x = \frac{\text{var } x}{\bar{x}^2} = \frac{\sum_{j=1}^{N_w} (x_j - \bar{x})^2}{N_w \bar{x}^2} \quad (3)$$

Where  $x_j$  denotes the pixel value. In single-stage filters,  $x$  corresponds to intensity  $I$ . The size of window depends on the application (e.g.  $3 \times 3, 5 \times 5, \dots$ ).

The ideal filter should eliminate the speckle so that the original signal  $\sigma$  is retrieved. In practice, its behaviour depends on the heterogeneity of the considered area.

First, two classes can be considered: 1) the homogeneous class corresponding to the area where  $\sigma$  is constant; 2) the heterogeneous class corresponding to the area where  $\sigma$  varies

and includes textured areas, edges, and point targets. The filter should have the following behaviour.

1. *Within the Homogeneous class:* The filter should restore  $\sigma$ . As the minimum variance unbiased estimator is the mean pixel value, the filter should assign to each pixel  $C$  the average of the pixels in a moving window centred at  $C$  for the image.
2. *Within the Heterogeneous class:* the filter should smooth the speckle and, at the same time, preserve edges and texture information ( $\sigma$  variations). This supposes that: i) The filter is based on good discriminators which allow a perfect separation between speckle and textural information; and ii) the conditions assumed for the filter establishment are satisfied.

In practice, these two conditions are not always satisfied. A third class is then pointed out where the filter is no longer reliable, and original pixel values are then preserved. In the case of an isolated point target, the filter should conserve the observed value  $I$ . This is also the case when there are a few scatterers within the resolution cells.

According to above consideration, the following classes are pointed out as a function of the coefficient of variation value.

1. Class to be averaged: if  $C_l \leq C_u$  then  $\hat{\sigma} = \bar{I}$ .
2. Class to be filters: if  $C_u < C_l < C_{\max}$ , then the filter should operate so that the more heterogeneous area [the larger  $C_l$ ], the less it has to be smoothed.
3. Class to be preserved: If  $C_l \geq C_{\max} \Rightarrow \hat{\sigma} = I$

Where  $C_l = \text{sqrt}(\bar{V}_x)$

The threshold determination is given by the following consideration (Lopes, et al., 1990a).

For an L-look image  $C_u = 1 / \sqrt{L}$  (an area is considered homogeneous). The threshold  $C_{\max}$  is more difficult to determine. A theoretical and experimental study should be developed to determine exactly the  $C_{\max}$  value as a function of the image patterns. One of the upper thresholds equal to  $\sqrt{1 + 2/L}$  for an intensity image has been obtained for likelihood ratio edge detection (Touzi, et al., 1988).

## 2.2 The de-speckling model

The approach of this chapter for reconstruction of backscattering coefficient ( $\hat{\sigma}$ ) is based on Bayes criterion relating the observed intensity  $I$  to the  $\sigma$  such that

$$P_{Ap}(\sigma | I) = P(I | \sigma)P_{\sigma}(\sigma) / P_l(I) \quad (4)$$

Where  $P_{Ap}(\sigma | I)$  is the a posterior conditional probability of  $\sigma$ , which has a particular value given  $I$ , and  $P(I | \sigma)$  is the likelihood function, which describes the effect of speckle during imaging. This is given by (Oliver, and Quegan, 2004).

$$P(I | \sigma) = \left(\frac{L}{\sigma}\right)^L \frac{I^{L-1}}{\Gamma(L)} \exp\left[-\frac{LI}{\sigma}\right] \quad (5)$$

for L-look SAR.  $P_{\sigma}(\sigma)$  is the a priori PDF that encapsulates prior knowledge about the RCS.

$P_l(I) = \int P(I | \sigma)P_{\sigma}(\sigma)d\sigma$  Only serves to normalize the expression and need not be included

specifically in most instances. Generally we wish to provide an estimate of  $\sigma$  that represents its most likely value given an observed  $I$ . This is equivalent to minimizing the log likelihood  $\lambda = \ln P_{AP}(\sigma | I)$  with respect to  $\sigma$ . Two types of maximum will be considered. If there is not prior knowledge of the form of  $P_{\sigma}(\sigma)$  we can only optimize with respect to the likelihood function in (4) leading to the Maximum Likelihood Estimate (MLE). However, if the form of the a priori PDF is known, the optimum is referred to as the maximum a posteriori (MAP) estimate. The latter is more precisely determined since it is based on more specific prior knowledge about the properties of the complete process.

The simplest approach to de-speckling is to average the intensity over several pixels within a window centred on a specific pixel. This is tantamount to assuming that the RCS is constant over the filter window. If this assumption is incorrect, the method is fundamentally flawed. The joint probability that all  $N$  pixels have this mean value is given by

$$P(\sigma | I_1, I_2, \dots, I_N) \propto \prod_{j=1}^N P(I_j | \sigma) = \prod_{j=1}^N \left( \frac{L}{\sigma} \right)^L \frac{I_j^{L-1}}{\Gamma(L)} \exp \left[ -\frac{LI_j}{\sigma} \right] \quad (6)$$

for L-look SAR, where pixels are assumed independent, The MLE for  $\sigma$  is then given by  $\sigma_{ML} = \bar{I}$  which is the average intensity over all the pixels in the window, corresponding to the multi-looking. Note that if this is applied to a single pixel the MLE is equal to the intensity of that pixel. Different values for the MLE in the de-speckling filters depend on constraints introduced by the model.

Multi-look de-speckling fails where the assumption of constant RCS within the window breaks down. The filter should then adapt to model the excess fluctuations compared with speckle within the window.

In this chapter, the approach that we developed for de-speckling is based on the least square method. If the original intensity of the centre pixel in a window is  $I$ , then its corrected value can be obtained by performing a first-order expansion in Taylor series about the local mean  $\bar{I}$  such that

$$\sigma_{LS} = \bar{I} + k(I - \bar{I}) + e \quad (7)$$

Where

$e$ : is the error that must be optimized;  $k$ : is selected to minimize  $e$ ;  $\sigma_{LS}$ : is the backscattering coefficient and  $\bar{I} = \frac{1}{N} \sum_{j=1}^N I_j$

But a better estimate for  $\sigma$  can be obtained, if we have a prior knowledge about the PDF of the RCS. The Bayes rule in (4) shows how this priori PDF can be used to provide a MAP reconstruction when combined with the likelihood function. The RCS of natural clutter can be well represented by a Gamma distribution of the form

$$P_{\sigma}(\sigma) = \left( \frac{v}{\mu} \right)^v \frac{\sigma^{v-1}}{\Gamma(v)} \exp \left[ -\frac{v\sigma}{\mu} \right] \quad (8)$$

Where  $\mu$  and  $v$  are the mean RCS and order parameter, respectively. These parameters cannot be measured directly and must be estimated from the data. Hence, estimates for  $\mu$  and  $v$  are obtained by passing a window over the original image and setting

$$\hat{\mu} = \bar{I} \quad \text{and} \quad \hat{v} = 1 / \bar{V}_\sigma = (1 + 1/L) / (\bar{V}_1 - 1/L)$$

The PDF of  $\sigma$  given intensity  $I$  when both likelihood and a priori PDF are available is given by

$$P_{AP}(\sigma | I) \propto P(I | \sigma)P_\sigma(\sigma) = \left(\frac{L}{\sigma}\right)^L \frac{I^{L-1}}{\Gamma(L)} \exp\left[-\frac{LI}{\sigma}\right] \left(\frac{v}{\mu}\right)^v \frac{\sigma^{v-1}}{\Gamma(v)} \exp\left[-\frac{v\sigma}{\mu}\right] \quad (9)$$

Hence, the log likelihood is given by

$$\begin{aligned} \lambda = \ln P(I | \sigma) + \ln P_\sigma(\sigma) = & L \ln L - L \ln \sigma + (L-1) \ln I - \ln \Gamma(L) - LI / \sigma \\ & + v \ln v - v \ln \mu + (v-1) \ln \sigma - \ln \Gamma(v) - \frac{v\sigma}{\mu} \end{aligned} \quad (10)$$

and the corresponding Gamma MAP solution for RCS (Kuan, et al., 1987; Oliver, 1991) is given by the quadratic:

$$\frac{v\sigma_{MAP}^2}{\mu} + (L+1-v)\sigma_{MAP} - LI = 0 \quad (11)$$

In regions of pure speckle, we would expect  $\bar{V}_1 \approx 1/L$  so that,  $\hat{v} = \infty$  and  $\sigma_{MAP} \approx \bar{I}$ . However, statistical fluctuations cause the estimate for  $\bar{V}_1$  to be less than  $1/L$ , so  $\hat{v}$  becomes negative. Again, the reconstruction can be improved when this occurs by setting  $\hat{v} = \infty$  so that  $\sigma_{MAP} = \bar{I}$ . In the opposite limit of small  $\hat{v}$ , provided that  $\mu/I \gg 4vL / (L+1)^2$ , the solution becomes  $\sigma_{MAP} = I / (1 + 1/L)$ .

In this chapter, we improve the Gamma-MAP filter by introducing an algorithm that detects and adapts to structural features, such as edges, lines, and points using least square method. The Gamma-MAP filter appears to give limited de-speckling performance. Large windows yield good speckle reduction over homogeneous regions but lead to artifacts over a distance equal to the filter dimension in the presence of strong features. This means that background clutter has excess variations in the precisely those areas where one would like to accurately defined. Small windows are largely free of these artifacts but give inadequate speckle reduction. In our algorithm, iteration leads to a considerable reduction in the speckle.

In principal, it should be possible to base the iteration process on updating the current pixel value, denoted by  $x$ , rather than the original intensity  $I$ . However, this demands knowledge of the conditional probability  $P(x | \sigma)$  relating the current pixel value  $x$  to the RCS  $\sigma$ . For residual speckle, this PDF would be expected to be gamma-distributed. Also any degradation in reconstruction will be retained, and probably exacerbated, during subsequent iterations. Thus it seems preferable to insist that the estimated RCS during each iteration should be consistent with the original intensity image described by the speckle conditional probability  $P(I | \sigma)$ . Though convergence is slower, there is less chance of progressively increasing radiometric distortion. Thus, we hope that  $x$  converges to  $\sigma$  and PDF for  $x$  converge to equation (8).

The equation (11) is nonlinear with respect to  $\sigma_{MAP}$ , we linearize equation (11) by Taylor series about the initial value for  $\sigma_{MAP}$  ( $\sigma_{MAP}^0$ ) as follows:

$$f(\sigma_{MAP}) = \frac{v\sigma_{MAP}^2}{\mu} + (L+1-v)\sigma_{MAP} - Lx = 0$$

$$f(\sigma_{MAP}) = f(\sigma_{MAP}^0) + \left(\frac{\partial f}{\partial \sigma_{MAP}}\right)^0 d\sigma_{MAP} + e = 0 \quad (12)$$

$$f(\sigma_{MAP}) = \left\{ \frac{v(\sigma_{MAP}^0)^2}{\mu} + (L+1-v)\sigma_{MAP}^0 - Lx \right\} + \left\{ \frac{2v\sigma_{MAP}^0}{\mu} + (L+1-v) \right\} d\sigma_{MAP} + e = 0$$

Where  $x$  is the current pixel value,  $\mu$  and  $v$  are estimated from the current iteration, so that  $\mu = \bar{x}$  and  $v = 1 / \bar{V}_x$ .

Thus, we can write  $N$  observation equations for pixels with intensity  $x_i$  ( $i=1, 2, \dots, N$ ) in the current iteration within the moving window with size of  $N=w \times w$  (here  $w=3$ ) that centred on a specific pixel as follows:

$$\left\{ \frac{v_w(\sigma_{MAP}^l)^2}{\mu_w} + (L+1-v_w)\sigma_{MAP}^l - Lx_i \right\} + \left\{ \frac{2v_w\sigma_{MAP}^l}{\mu_w} + (L+1-v_w) \right\} d\sigma_{MAP} + e = 0; \quad i=1, 2, \dots, N \quad (13)$$

Fig 1 shows the process of the de-speckling model.

According to the diagram of Fig 1, a moving window,  $W$ , is placed in the top left centre of the SAR image to be filtered (Fig 2) and the mean and the standard deviation values of the pixels within the moving window centred on a specific pixel are computed. Based on the pixels in the window, a linear observation equation system is performed for all pixels in the window using the observation equation (13). The system is solved by using the least square method (LSM) to determine the correction  $d\sigma_{MAP}$ . This correction is added to the value,  $\sigma_{MAP}^l$ , and the new value,  $\sigma_{MAP}^{II}$ , is replaced in the output image (filtered image) at the point that is corresponding to the location of the specific pixel (see Fig 2).

The proposed algorithm in Fig 1 proceeds as following steps:

Step 1: Initialization stage

1. Set the parameters and consider the  $l$ th pixel with intensity  $I_l$

Step 2: Perform intensity update (Filtered image)

1. Compute the mean and the standard deviation values of the moving window  $W$  centred in the  $l$ th pixel
2. Perform the linear observation equation system based on the equation (13) for all elements in the window  $W$
3. Using the least square method to determine the correction  $d\sigma_{MAP}$
4. Compute the new value  $\sigma_{MAP}^{II}$  ( $\sigma_{MAP}^{II} = \sigma_{MAP}^l + d\sigma_{MAP}$ ) for  $l$ th pixel
5. Increment  $l$  and go to step 2 until  $l = M_{im} \times N_{im}$ , ( $M_{im} \times N_{im}$  is the size of the image)

Step 3: Acceptance/ Rejection stage

1. Evaluation of the ratio of the original intensity image,  $I$ , to the derived RCS image,  $x_2$ , (Ratio image)
2. Estimate the mean,  $\bar{r}$ , and standard deviation,  $SD[r]$ , for the Ratio image as follows

$$\bar{r} = \frac{1}{N_{im} \times M_{im}} \sum_{l=1}^{N_{im} \times M_{im}} r_l \quad \text{and} \quad SD[r] = \sqrt{\frac{1}{N_{im} \times M_{im}} \sum_{l=1}^{N_{im} \times M_{im}} (r_l - 1)^2} \quad (14)$$

Where  $r_l = I_l / (x_2)_l$  is the ratio of the pixel intensity  $I_l$  to the derived RCS  $(x_2)_l$  at pixel  $l$ .

3. IF {  $\bar{r}$  and  $SD[r]$  values are remained almost the same in the previous iteration } THEN {stop the algorithm}  
 ELSE {continue and go to step 1}.

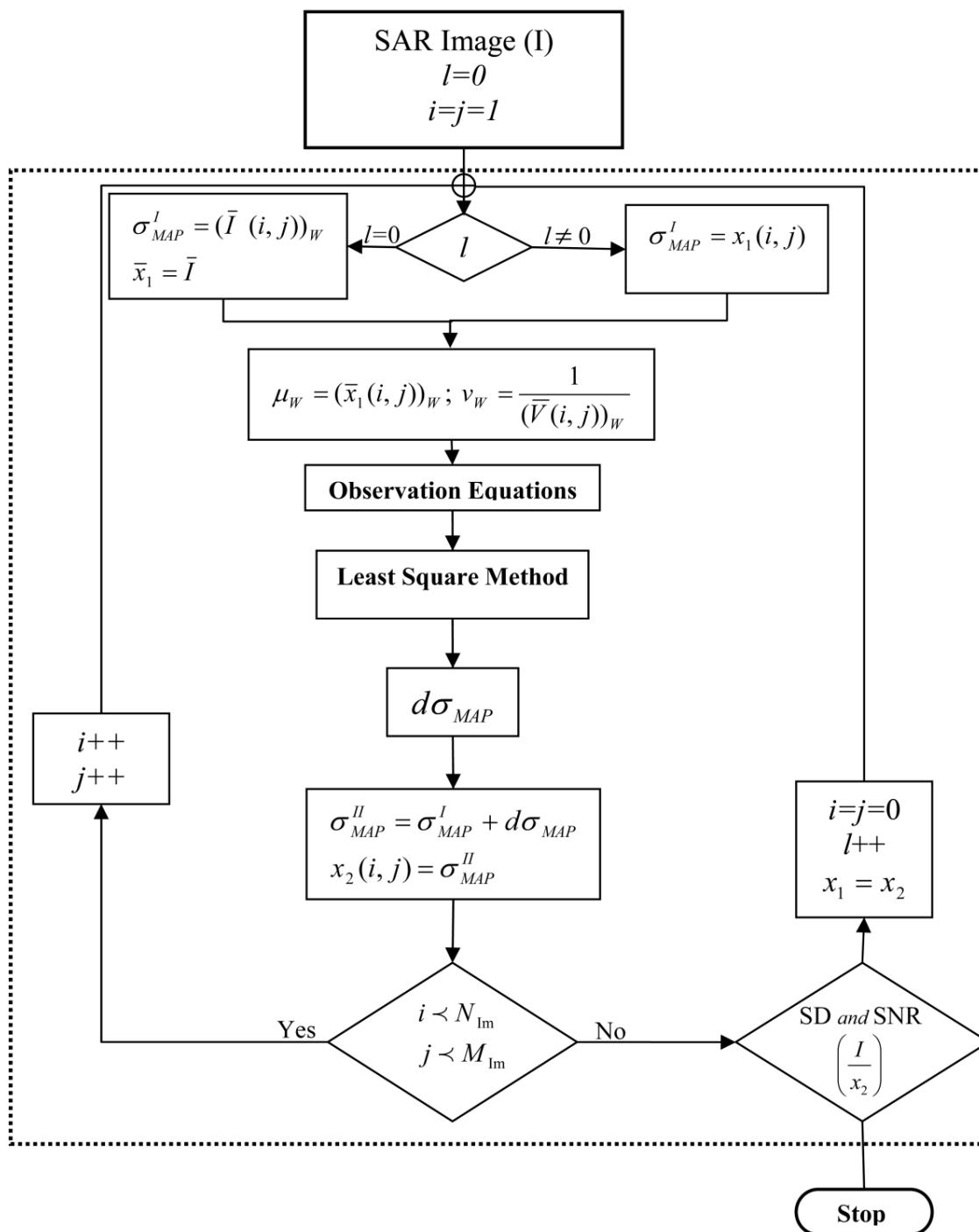


Fig. 1. The flowchart of the de-speckling model

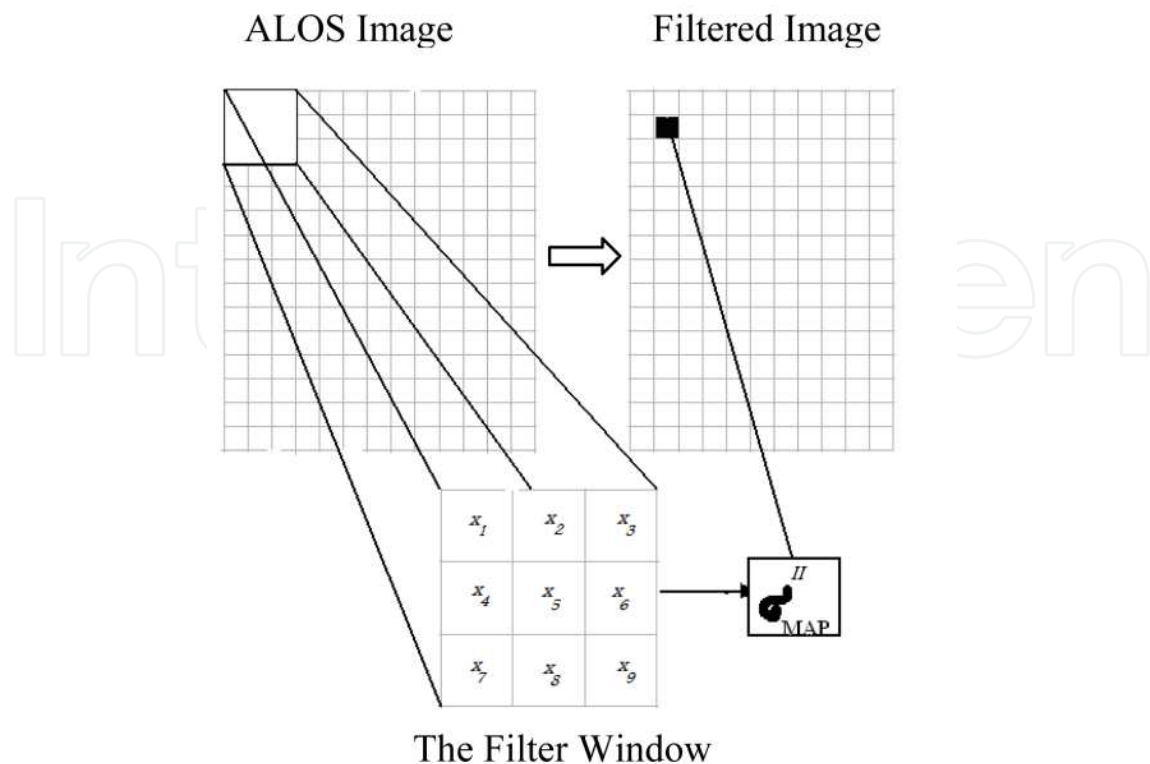


Fig. 2. Operation of the moving window with size of  $3 \times 3$

### 3. Methodology and implementation

The methodology used for the forest inventory is distinct according to the vegetation type. In forest areas, different parameters are measured namely: diameter at breast height (DBH), total and commercial height, crown cover percent, and location of each plots. Total height is the height from the upper branches of a tree to the ground and the commercial height is the height of the main trunk of a tree. The crown cover percent is also percent of the number of trees in a hectare. We measured the total height during the field survey and used it in the allometric equation. In addition, the identification of botanical species is also conducted.

The field work consists of collecting some bio-physical and dendrometric parameters which allowed the biomass estimation of the plots and the physiognomic-structural characterization of the different vegetation types considered. The precise geographic coordinates of each plot are obtained using a high-precision Global Positioning System (GPS), which allows the localization of each plots, in the previously geo-referenced images.

The study area is located in the northern forests of Iran around the Rezvanshahr city (Fig. 3(a)). The dominant trees of these forests are: *Maple*, *Alder*, *Conifer*, *Beech*, *Hornbeam*, *Azedarach* and *Acorn*. Remote sensing data also consist of: AVNIR-2 and PRISM images from ALOS and a JERS-1 image. The JERS-1 image has a spatial resolution of approximately 13m and, AVNIR-2 and PRISM images have the spatial resolutions of 10m and 2.5m respectively. According to Fig. 3(b), the ground data is collected at five plots in the study area. Each plot



Fig. 3. (a) Study area of the north of Iran, (b) Plots in the study area indicated with circles.

was a square with size of 50m×50m with 25 subplots with size of 10m×10m approximately. The minimum DBH considered was of 37cm. The plots were mostly covered by two classes: Acorn and Azedarach. The distribution of the classes with numbers of stands where

measured in each subplots are shown in Table 1. Table 1 summarizes some of the ground measurements and resulting calculations.

The biomass in Table 1 is modelled based on the direct DBH and the total height measurements performed during the field survey and included afterwards in the general allometric equation (15) (Brown et al., 1989).

$$biomass = 0.044 \times ((DBH)^2 \times height)^{0.9719} \quad (15)$$

Where: DBH is in cm, height is in m, and biomass is in kg/ tree.

For speckle reduction in the SAR image, the de-speckling model apply on the JERS-1 image of the study area and then its result is compared with several of the most widely used adaptive filters including the Kuan, Gamma, Lee and Frost filters.

In order to investigate the performance of the model, we use some quantitative criteria including speckle smoothing measures and texture preservation to evaluate the performance of the model.

Plot	# of subplots for Acorn Azedarach		Mean height (m)	Mean DBH (cm)	Mean Biomass (ton/tree)	# of stands for Acorn Azedar		Total mean biomass (ton) for Acorn Azedarach	
1	20	5	28.5	40	1.484	15	05	26.712	07.420
2	07	18	34	55	3.275	08	13	25.960	42.575
3	19	06	26.5	35	1.066	24	10	25.584	10.660
4	15	10	29	45	1.897	14	09	26.558	17.073
5	04	21	27.5	38	2.373	06	24	14.238	56.952

Table 1. Field plots characteristics

The ratio of the original intensity image to the filtered image enable us to determine the extent to which the reconstruction filter introduces radiometric distortion so that the reconstruction departs from the expected speckle statistics. The mean and standard deviation (SD) can then be estimated over the ratio images. When the mean value differs significantly from one, it is an indication of radiometric distortion. If the reconstruction follows the original image too closely, the standard deviation would be expected to have a lower value than predicted. It would be larger than predicted if the reconstruction fails to follow genuine RCS variations. This provides a simple test that can be applied to any form of RCS reconstruction filters. Table 2, columns 2 and 3, shows the mean and standard deviation values of the ratio images for comparison of the filters.

Algorithm	Ratio image		Filtered image	
	Mean	S. D	ENL	VTO
<i>The model</i>	0.991	0.037	26.78	643.12
Kuan	0.968	0.195	4.96	90.12
Gamma	0.968	0.195	4.96	335.12
Enhanced Lee	0.968	0.195	4.96	234.26
Enhanced Frost	0.968	0.195	16.15	401.32

Table 2. Comparison of the mean and SD in the ratio images, ENL and variance texture operator of the filtered images

According to Gagnon and Jouan (1997), Equivalent number of Looks (ENL) is often used to estimate the speckle noise level in a SAR image and is equivalent to the number of independent intensity values that are used per pixel.

It is the mean-to-standard deviation ratio, which is a measure of the signal-to-noise ratio and is defined over a uniform area as follows:

$$ENL = \frac{(\text{mean}^2)_{\text{UniformArea}}}{(\text{variance})_{\text{UniformArea}}} \quad (16)$$

ENL is used to measure the degree of speckle reduction in this study. The higher the ENL value concludes the stronger the speckle reduction.

Texture preservation is another measure that is important in a SAR image for interpretation and classification. Therefore, the texture preserving capability should play an important role in measuring the performance of a speckle filter. A second-order texture, variance (Iron & Petersen, 1981), is used to measure the retention of texture information in the original and the filtered images.

The ENL and the second-order texture values of the filtered images are shown in Table 2 columns 4 and 5 respectively. Of the four commonly used filters, Enhanced Frost filter has higher speckle-smoothing capabilities than Kuan, Gamma and Enhanced Lee filters. The ENL value of the model is 26.78 that it is comparable to Enhanced Frost filter. According column 5, Variance Texture Operator (VTO), in Table 2, the texture preservation of the proposed filter is better than, or comparable to, those of the commonly used speckle filters. We concluded the model is slightly better than the commonly used filters in terms of preserving details in forestry areas. Furthermore, the model also affects in smoothing speckles. This improvement in the accuracy of the speckle reduction can be played an important role in the forest biomass estimation.

After reduction the speckle noise, the texture of SAR image must be measured. Of the many describing texture methods, the grey-level co-occurrence matrix (GLCM) is the most common (Marceau et al., 1990; Smith et al., 2002; Zhang et al., 2003) in remote sensing.

Nine texture measures are calculated from the GLCM for a moving window with size of 5×5 pixels that centred in pixel  $i, j$  of the de-speckled JERS-1 image. After the Gram-Schmidt process, just four texture measures: *contrast*, *correlation*, *maximum probability* and *standard-deviation* are selected as the optimum measures in this area.

The PRISM image is transformed in the universal transverse Mercator (UTM) projection with a WGS84 datum based on the GPS measurements and is used as the base map. Two GPSs measured the coordinates of points along the roads of the study area. To place all data sets in a unified coordinate system, the AVNIR and JERS-1 image are registered to this map. The co-registered and geo-referenced data sets contain PRISM, AVNIR and SAR images are used to extract intensity values and texture measures respectively.

#### 4. Experimental results

Intensity value and texture measures from the co-registered and geo-referenced data sets are used in the algorithm to estimate the forest biomass. The data sets are related to the forest biomass through a classification analysis. The correspondence between the data sets and ground plots is made using PCI Geomatica software, where the ground plot GPS locations are superimposed on the data set. For each selected pixel (or point) from data set, a window

with size of 5×5 pixels around the point is used and the average intensity values for the PRISM and three channels of the AVNIR images with four texture values of the JERS-1 image are calculated. Thus each selected point contains a vector with eight attributes where the first four elements are the average intensity values and the second four elements are the texture measures values. These vectors of data set construct the feature space. The vectors belong to the pixels of the ground plots and subplots are used as training patterns in the classification process.

The classification analysis is done with a MLPNN. A multi layers neural network is made up of sets of neurons assembled in a logical way and constituting several layers. Three distinct types of layers are present in the MLPNN. The input layer is not itself a processing layer but is simply a set of neurons acting as source nodes which supply input feature vector components to the second layer. Typically, the number of neurons in the input layer is equal to the dimensionality of the input feature vector. Then there is one or more hidden layers, each of these layers comprising a given number of neurons called hidden neurons. Finally, the output layer provides the response of neural network to the pattern vector submitted in the input layer. The number of neurons in this layer corresponds to the number of classes that the neural network should differentiate (Haykin, 1999; Miller et al., 1995; .

The network that is used in this study arrange in layers as following. The number of neurons in the output layer is taken to be equal to the number of classes desired for the classification. Here, the output layer of the network used to categorize the image in five classes should contain five neurons. The input layer contains eight neurons corresponding to the number of attributes in the input vectors. The input vector to the network for pixel  $i$  of the data sets is the form  $v_{i_{os}} = \{v_{i1}, v_{i2}, \dots v_{i8}\}$ . Where the first four elements belong to the intensity values of PRISM and AVNIR images and the second four elements belong to the texture measures of JERS-1 image for a window with size of 5×5 around pixel  $i$  of the geo-referenced data sets. After the determination of the input layer, the number of hidden layers required as well as the number of neurons in these layers still needs to be decided upon. An important result, established by the Russian mathematician Kolmogorov in the 1950s, states that any discriminate function can be derived by a three-layer feed-forward neural network (Duda, 2001). Increasing the number of hidden layers can then improve the accuracy of the classification, pick up some special requirements of the recognition procedure during the training or enable a practical implementation of the network. However, a network with more than one hidden layer is more prone to be poorly trained than one with only one hidden layer.

Thus, a three-layer neural network with the structure 8-10-5 (eight input neurons, ten hidden neurons and five output neurons) is used to classify the data sets into five classes.

Training the neural network involves tuning all the synaptic weights so that the network learns to recognize given patterns or classes of samples sharing similar properties. The learning stage is critical for effective classification and the success of an approach by neural networks depends mainly on this phase. The network is trained by using back-propagation rule (Paola & Schowengerdt, 1995). After training the network, the parameters are selected as: Momentum value 0.9, Learning rate 0.1, and the number of iteration 2000. The numbers of training data are 200 patterns of the subplots that are selected randomly from the classes, in which each class is represented with at least 40 patterns. The set of training patterns is presented repeatedly to the neural network until it has learnt to recognize them. A training pattern is said to have been learnt when the absolute difference between the output of each

output neuron and its desired value is less than a given threshold. Indeed, it is pointless to train the network to reach the target outputs 0 or 1 since the sigmoid function never attains its minimum and maximum (Masters, 1993). For classification of data sets into five classes, the threshold is set to 0.4. The network is trained when all training patterns have been learnt. Once the network is trained, the weights of the network are applied on the data sets to classify into five classes: class1 *Azedarach*, class2 *Acorn*, class3 *Beech*, class4 *Grassland* and class5 *None*. The result of the classified image is shown in Fig. 4.

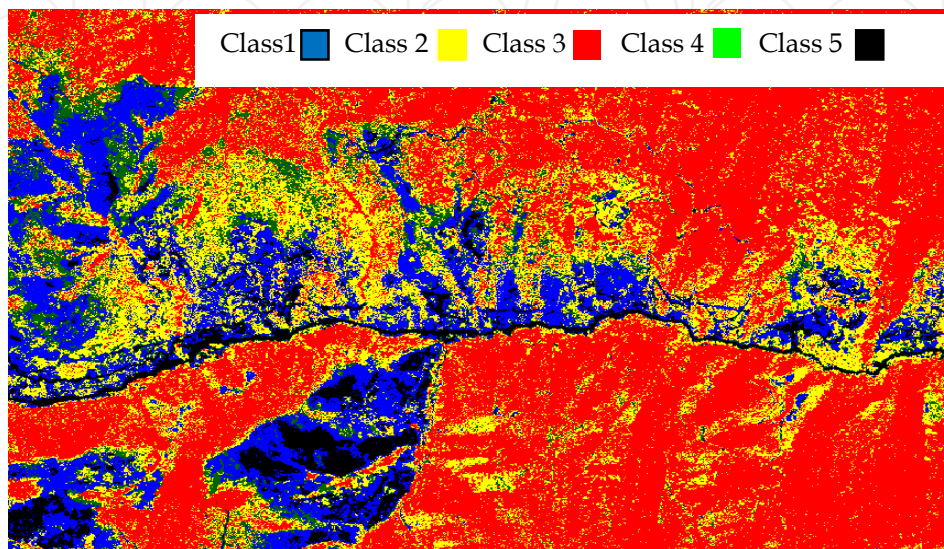


Fig. 4. The classified image with MLPNN.

After classification, it is needed to determine the degree of classification accuracy. The most commonly used method of representing the degree of accuracy of a classification is to build confusion matrix.

The confusion matrix is usually constructed by a test sample of patterns for each of the five classes. A set of test sample with 105 patterns based on the ground truth collection were randomly selected in the classified image for accuracy assessment. The values 70% and 65% are achieved for overall accuracy and kappa coefficient respectively. One reason for misclassification can be due to poor selection of training areas, so that some training patterns don't accurately reflect the characteristics of the classes used. Another reason can be due to poor selection of land cover categories, resulting in correct classification of areas from the point of view of the network, but not from that of the user. Thus the classification accuracy can be improved by redefining the training patterns and land cover categories.

In order to show the texture of SAR image and the neural network classifier improve the accuracy of the classification and then forest biomass estimation, we employ the Maximum Likelihood (ML) classifier method using only the intensity values of the PRISM and AVNIR images. The overall classification accuracy of 57% is achieved with ML classifier. The accuracy of 70% with the neural network is significantly better than the accuracy of 57% with ML.

In comparison between the MLPNN and ML classifiers, the advantages of MLPNN that is used in this study are:

- i. It can accept all kind of numerical inputs whether or not these conform to statistical distribution or not.

ii. It can recognize inputs that are similar to those which have been used to train them. Because the network consists of a number of layers of neurons, it is tolerant to noise present in the training patterns.

Thus, we can estimate the forest biomass of the classes in the classified image which has been classified based on the SAR image texture and the MLPNN classifier. We also evaluate the biomass for two classes based on the allometric equation (15) for the classic method based on the ML classifier and the proposed method. The results are shown in Table 3, where the classic method and the proposed method have been applied in the classified image to estimate the biomass for two classes.

	<b>The classic method</b>		<b>The proposed method</b>	
	Acorn	Azedarach	Acorn	Azedarach
Area (ha)	853.217	1129.552	937.312	1241.320
Mean height (m)	34	28.5	34	28.5
Mean DBH (cm)	55	45	55	45
# of tree (ha)	34	23	34	23
Mean biomass (kg/tree)	3272	1861.99	3272	1861.99
Total biomass (tons/ha)	94918.85	48374.08	104274.085	53160.484

Table 3. Estimated biomass for the classic method and the proposed method by both optical and sar data.

For the accuracy assessment of the proposed method, Table 4 shows how well the results agree with the ground measurements results from Table 1, when the classic method and the proposed method are used for biomass estimation. Table 4 shows the estimated biomass when both methods are used. The root mean square error (RMSE) of estimated biomass with both methods is indicated in the table. The RMSE values is decreased when the model is used (RMSE=2.175 ton) compared the classic method (RMSE=5.34 ton).

Plot	Measured biomass (ton) for		<b>The classic method</b> Estimated biomass (ton) for		<b>The proposed method</b> Estimated biomass (ton) for	
	Azedarach	Acorn	Azedarach	Acorn	Azedarach	Acorn
1	26.712	07.42	29.13	10.40	27.43	09.12
2	25.960	42.575	30.40	46.39	27.13	41.43
3	25.584	10.660	18.13	06.43	23.32	08.86
4	26.558	17.073	22.13	24.32	23.16	21.36
5	14.238	56.952	17.43	66.13	15.29	58.56
<i>RMSE</i>			<b>4.71</b>	<b>5.97</b>	<b>1.97</b>	<b>2.38</b>
<i>Mean RMSE</i>				<b>5.34</b>		<b>2.17</b>

Table 4. Accuracy assessment for the classic method and the proposed model using the ground measurements from Table 1.

From the above paragraphs, the accuracy of the proposed method is better than, or comparable to, the classic method used for biomass estimation. We conclude using both

optical image and SAR image texture in a non-linear classifier method, neural network, significantly improve the accuracy of the forest biomass estimation.

## 5. Discussion

It is often difficult to transfer one model developed in a specific study area to other study areas because of the limitation of the model itself and the nature of remotely sensed data. Foody (Foody et al., 2003) discussed the problems encountered in model transfer. Many factors, such as uncertainties in the remotely sensed data (image preprocessing and different stages of processing), AGB calculation based on the field measurements, the disparity between remote sensing acquisition date and field data collection, and the size of sample plot compared with the spatial resolution of remotely sensed data, could affect the success of model transferability. Each model has its limitation and optimal scale for implementation. Models developed in one study area may be transferred to (1) across-scene data, which have similar environmental conditions and landscape complexity, to estimate AGB in a large area; and (2) multi-temporal data of the same study area for AGB dynamical analysis if the atmospheric calibration is accurately implemented. The spectral signatures, vegetation indices, and textures are often dependent on the image scale and environmental conditions. Caution must be taken to ensure that there is consistency between the images used in scale, atmospheric and environmental conditions. Calibration and validation of the estimated results may be necessary using reference data when using transferred models.

The data sources used for AGB estimation may include field-measured sample data, remotely sensed data, and ancillary data. A high-quality sample dataset is a prerequisite for developing AGB estimation models as well as for validation or assessment of the estimated results. Direct measurement of AGB in the field is very difficult. In general, AGB is calculated using the allometric equations based on measured DBH and/or height, or from the conversion of forest stocking volume. These methods generate many uncertainties and calibration or validation of the calculated AGB is necessary. Previous research has discussed the uncertainties of using the allometric equations (Brown & Gaston, 1995; Keller et al., 2001; Ketterings, 2001; Fearnside, 1992) and of conversion from stocking volume (Masters, 1993). It is important to ensure that the remote sensing data, ancillary data, and sample plots are accurately registered when ancillary data are used for AGB estimation. Understanding and identifying the sources of uncertainties and then devoting efforts to improving them are keys to a successful AGB estimation. More research is needed in the future for reducing the uncertainties from different sources in the AGB estimation procedure. Many remote sensing variables, including spectral signatures, vegetation indices, transformed images, and textures, may become potential variables for AGB estimation. However, not all variables are required because some are weakly related to AGB or they have high correlation with each other. Hence, selection of the most suitable variables is a critical step for developing an AGB estimation model. In general, vegetation indices can partially reduce the impacts on reflectance caused by environmental conditions and shadows, thus improving correlation between AGB and vegetation indices, especially in those sites with complex vegetation stand structures (LU, 2004). On the other hand, texture is an important variable for improving AGB estimation performance. One critical step is to identify suitable textures that are strongly related to AGB but are weakly related to each other. However, selection of suitable textures for AGB estimation is still a challenging task because textures vary with the

characteristics of the landscape under investigation and images used. Identifying suitable textures involves the determination of appropriate texture measures, moving window sizes, image bands, and so on (Franklin & Hiernaux, 1991). Not all texture measures can effectively extract biomass information. Even for the same texture measure, selecting an appropriate window size and image band is crucial. A small window size, such as 3×3, often exaggerates the difference within the moving windows, increasing the noise content on the texture image. On the other hand, too large a window size, such as 11×11 or larger, cannot effectively extract texture information due to smoothing the textural variation too much. Also, a large window size implies more processing time. In practice, it is still difficult to identify which texture measures, window sizes, and image bands are best suited to a specific research topic and there is a lack of guidelines on how to select an appropriate texture. More research is needed to develop suitable techniques for identification of the most suitable textures for biomass estimation.

In addition to remotely sensed above ground biomass estimation in data, different soil conditions, terrain factors, and climatic conditions may influence AGB estimation because they affect AGB accumulation rates and development of forest stand structures. Incorporation of these ancillary data and remote sensing data may improve AGB estimation performance. Geographical Information System (GIS) techniques can be useful in developing advanced models through the combination of remote sensing and ancillary data.

## 6. Conclusion

In this chapter, we proposed a method for forest biomass estimation. One speckle noise model was used for reducing the speckle noise in SAR images. The speckle model was slightly better than the commonly used filters in terms of preserving details in forestry areas. A combination of spectral responses from optical images and textures from SAR images improved biomass estimation performance comparing pure spectral responses or textures. Intensity values of ALOS-AVNIR-2 and PRISM images and texture features of JERS-1 image were used in a multilayer perceptron neural network (MLPNN) that relates them to the forest variable measurements on the ground. We showed the biomass estimation accuracy was significantly improved when MLPNN was used in comparison to estimating the biomass by using classic method only. The RMSE values was decreased when the proposed method was used (RMSE=2.175 ton) compared the classic method (RMSE=5.34 ton).

## 7. References

- Achim, A.; Kuruoglu, E.E. & Zerubia, J. (2006). SAR image filtering based on the heavy-tailed Rayleigh model, *IEEE Trans. Image Processing*, Vol. 15, no.9, pp. 2686- 2693.
- Aiazzi, B.; Alparone, L.; Baronti, S. & Carla, R. (1997). Adaptive texture-preserving filtering of multitemporal ERS-1 images. *Proceedings of IGARSS' 97, IEEE International Geoscience and Remote Sensing Symposium*, 3–8 August 1997 (Singapore: IGARSS), pp. 2066–2068.
- Amini, J. & Sumantyo, J.T.S. (2009). Employing a method on SAR and Optical Images for Forest Biomass Estimation, *IEEE Trans. on Geoscience and remote sensing*, Vol. 47, No. 12. pp. 4020-4026.

- Baraldi, A. & Parmiggiani, F. (1995). A refined Gamma Map SAR speckle filter with improved geometrical adaptivity, *IEEE Trans. Geosci. Remote Sensing*, 33, pp. 1245–1257.
- Brown, S.; Gillespie, A.J.R. & Lugo, A.E. (1989). Biomass estimation methods for tropical forests with applications to forest inventory data, *Forest Science*, 35, pp. 881–902.
- Brown, S. & Gaston, G. (1995). Use of forest inventories and geographic information systems to estimate biomass density of tropical forests: application to tropical Africa, *Environmental Monitoring and Assessment*, 38, pp. 157–168.
- Crimmins, T. R. (1985), Geometric filter for speckle reduction. *Applied Optics*, 24, 1438–1443.
- Dobson, M.C.; Ulaby, F.T.; LeToan, T.; Beaudoin, A; Kasischke, E.S. & Christensen, N. (1992). Dependence of radar backscatter on coniferous forest biomass, *IEEE Trans Geosc.Remote Sensing*, Vol. 30, no. 2, pp. 412 – 415.
- Dong, Y.; Milne, A.K. & Forester, B.C. (2001). Toward edge sharpening: a SAR speckle filtering algorithm, *IEEE Trans. Geosci. Remote Sensing*, Vol. 39, no.4, pp. 851–863.
- Duda, R.O.; Hart, P.E. & Stork, D.G. (2001). *Pattern Classification, 2<sup>nd</sup> edition*, New York: John Wiley and Sons.
- Franklin, J. & Hiernaux, P. (1991). Estimating foliage and woody biomass in Sahelian and Sudanian woodlands using a remote sensing model, *Int. J. Remote Sensing*, 12, pp. 1387–1404.
- Foody, G.M.; Boyd, D.S. & Cutler, M. (2003). Predictive relations of tropical forest biomass from Landsat TM data and their transferability between regions, *Remote Sensing of Environment*, 85, pp. 463–474.
- Frost, V.S; Stiles, J.A; Schanmugan, K.S. & Holzman, J.C. (1982). A model for radar images and its application to adaptive digital filtering of multiplicative noise, *IEEE Trans. on Pattern Analysis and Machine Intelligence*, 4, pp. 157–166.
- Fearnside, P.M. (1992). Forest biomass in Brazilian Amazonia: comments on the estimate by Brown and Lugo, *Interciencia*, 17, pp. 19–27.
- Fukuda, S. & Hirosawa, H. (1998). Suppression of speckle in synthetic aperture radar images using wavelets. *International Journal of Remote Sensing*, 19, pp. 507–519.
- Gagnon, L. & Jouan, A. (1997). Speckle filtering of SAR images—a comparative study between complex- wavelet-based and standard filters, *Proceedings of SPIE Wavelet Applications in Signal and Image Processing*, SPIE volume 3169, pp. 80–91.
- Gagnon, L. & Jouan, A. (1997). Speckle filtering of SAR images—a comparative study between complex- wavelet-based and standard filters, *Proceedings of SPIE Wavelet Applications in Signal and Image Processing*, 1997, SPIE volume 3169, pp. 80–91.
- Hagg, W. & Sties, M. (1994). Efficient speckle filtering of SAR images, *Proceedings of IGARSS' 94*, 1994 (California: IGARSS), pp. 2140–2142.
- Haykin, S. (1999). *Neural networks: A Comprehensive Foundation, 2<sup>nd</sup> edition*, Upper Saddle River, New Jersey: Prentice Hall.
- Iron, J.R. & Petersen, G.W. (1981). Texture transforms of remote sensing data, *Remote sensing of environment*, Vol. 11, pp. 359–370.

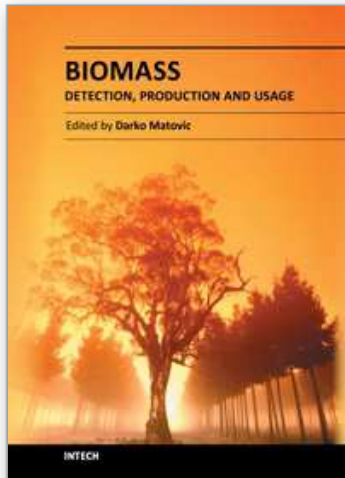
- Keller, M.; Palace, M.; & Hurtt, G. (2001). Biomass estimation in the Tapajos National Forest, Brazil, Examination of sampling and allometric uncertainties, *Forest Ecology and Management*, 154, pp. 371–382.
- Ketterings, Q.M.; Coe, C.; Van noordwijk, M; Ambagau, K. & Palm, C.A. (2001). Reducing uncertainty in the use of allometric biomass equations for predicting aboveground tree biomass in mixed secondary forests, *Forest Ecology and Management*, 146, pp. 199–209.
- Kuan, D. T.; Sawchuk, A. A.; Strand, T. C. & Chavel, P. (1987). Adaptive restoration of images with speckle, *IEEE Transactions on Acoustics, Speech, and Signal Processing*, 35, pp. 373–383.
- Kuan, D.T.; Sawchuk, A.A; Strand, T.C. & Chavel, P. (1987). Adaptive restoration of images with speckle, *IEEE Trans. on Acoustics, Speech, and Signal Processing*, 35, pp. 373–383.
- Lu, D. (2005). Aboveground biomass estimation using Landsat TM data in the Brazilian Amazon Basin, *Int. J. Remote Sensing*, 26, pp. 2509–2525.
- Lee, J.S. (1980). Digital image enhancement and noise filtering by use of local statistics, *IEEE Trans. on Pattern Analysis and Machine Intelligence*, 2, pp. 165–168.
- Lopes, A.; Touzi, R; Nezry, E. (1990a). Adaptive speckle filters and scene heterogeneity, *IEEE Trans. Geosci. Remote Sensing*, Vol. 28, No. 6, pp. 1953–1962.
- Lopes, A.; Nezry, E.; Touzi, R & Laur, E. (1990b). Maximum a posteriori speckle filtering and first order texture models in SAR images, *Proceedings of IGARSS' 90*, May 1990, vol. 3 (Maryland: IGARSS), pp. 2409–2412.
- Lu, D.; Mausel, P.; Brondizio, E. & Moran, E. (2004). Relationships between forest stand parameters and Landsat Thematic Mapper spectral responses in the Brazilian Amazon Basin, *Forest Ecology and Management*, 198, pp. 149–167.
- Li, C. (1988). Two adaptive filters for speckle reduction in SAR images by using the variance ratio. *International Journal of Remote Sensing*, 9, pp. 641–653.
- Lin, Q. & Allebach, J. P. (1990). Combating speckle in SAR images: vector filtering and sequential classification based on a multiplicative noise model. *IEEE Transactions on Geoscience and Remote Sensing*, 28, pp. 647–653.
- Lopes, A.; Touzi, R.; Nezry, E. (1990a). Adaptive speckle filters and scene heterogeneity. *IEEE Transactions on Geoscience and Remote Sensing*, Vol. 28, No. 6, pp. 1953–1962.
- Marceau, D.J; Howarth, P.J.; Dubois, J.M. & Gratton, D.J. (1990). Evaluation of the grey-level co-occurrence matrix method for land-cover classification using SPOT imagery, *IEEE Trans. Geosci. Remote Sensing*, 28, pp. 513–519, 1990.
- Miller, D.M.; Kaminsky, E.J. & Rana, S. (1995). "Neural network classification of remote sensing data", *Computers and Geosciences*, Vol. 21, pp: 377-386.
- Masters, T. (1993). *Practical Neural Network Recipes in C++*, San Diego: Academic Press.
- Mallat, S. G. (1989a). A theory for multiresolution signal decomposition: the wavelet representation. *IEEE Transactions on Pattern Analysis and Machine Intelligence*, 11, pp. 674–693.
- Mallat, S. G. (1989b). Multifrequency channel decomposition of images and wavelet models. *IEEE Transactions on Acoustics, Speech, and Signal Processing*, 37, p. 2091–2110.
- Martin, F. J.; & Turner, R. W. (1993). SAR speckle reduction by weighted filtering. *International Journal of Remote Sensing*, 14, pp. 1759–1774.

- Nelson, R.; Krabill, W. & Tonelli, J. (1998). Estimating forest biomass and volume using airborne laser data, *Remote Sensing of Environment*, 24, pp. 247-267.
- Nezry, E.; Lopes, A. & Touzi, R. (1991). Detection of structural and textural features for SAR images filtering, *Proceedings of IGARSS' 91*, June 1991, vol. 3 (Helsinki: IGARSS), pp. 2169-2172.
- Oliver C. & Quegan S. (2004). *Understanding Synthetic Aperture Radar Images*, Scitech Pub.,
- Oliver, C. J. (1991). Review article-Information from SAR images, *J. Phys. D: Appl. Phys.*, Vol. 24, pp. 1493-1514.
- Paola, J. & Schowengerdt, R.A. (1995). "A review and analysis of back-propagation neural networks for classification of remotely-sensed multi-spectral imagery", *Int. J. Remote Sensing*, Vol. 16, pp: 3033-3058.
- Porcello, L. J.; Massey, N. G.; Innes, R. B.; & Marks, J. M. (1976). Speckle reduction in synthetic radars. *Journal of the Optical Society of America*, 66, pp. 1305-1311.
- Quinones, M.J. & Hoekman, D.H. (2004). Exploration of factors limiting biomass estimation by polarimetric radar in tropical forests, *IEEE Trans. Geosci. Remote Sensing*, Vol. 42, nu.1, pp. 86 - 104.
- Rignot, E.J.; Zimmermann, R. & van Zyl, J.J. (1995). Spaceborne applications of P band imaging radars for measuring forest biomass, *IEEE Trans. Geosci. Remote Sensing*, Vol. 33, no. 5, pp. 1162 - 1169.
- Rignot, E.; Way, J; Williams, C. & Viereck, L. (1994). Radar estimates of aboveground biomass in boreal forests of interior Alaska, *IEEE Trans. Geosci. Remote Sensing*, Vol. 32, no5, pp. 1117 - 1124.
- Rao, P. V. N.; Vidyadhar, M. S. R. R.; Rao, T. C. M.; & Venkataratnam, L. (1995). An adaptive filter for speckle suppression in synthetic aperture radar images. *International Journal of Remote Sensing*, 16, pp. 877-889.
- Sumantyo, J.T.S. & Amini, J. (2008). A model for removal of speckle noise in SAR images (ALOS PALSAR), *Canadian Journal of Remote Sensing*, Vol. 34, No. 6, pp. 503-515.
- Simard, M.; Degrandi, G.; Thomson, P. B. & Benie, G. B. (1998). Analysis of speckle noise contribution on wavelet decomposition of SAR images. *IEEE Transactions on Geoscience and Remote Sensing*, 36, pp. 1953-1962.
- Smith, A.M.S.; Wooster, W.J; Powell, A.K. & Usher, D. (2002). Texture based feature extraction: application to burn scar detection in Earth observation satellite sensor imagery, *Int. J. Remote Sensing*, 23, pp. 1733-1739.
- Sader, S.A. ; Waide, R.B.; Lawrence, W.T. & Joyce, A.T. (1989). Tropical forest biomass and successional age class relationships to a vegetation index derived from Landsat TM data, *Remote Sensing of Environment*, 28, pp. 143-156.
- Steininger, M.K. (2000). Satellite estimation of tropical secondary forest aboveground biomass data from Brazil and Bolivia, *Int. J. Remote Sensing*, 21, pp. 1139-1157.
- Touzi, R.; Lopes, A.; & Bousquet, P. (1988). A statistical and geometrical edge detector for SAR images, *IEEE Trans. on Geoscience and Remote sensing*, Vol. 26, pp. 764-773.
- Walkup, J. F. & Choens, R. C. (1974). Image processing in signal dependent noise. *Optical Engineering*, 13, pp. 250-266.

- Woods, J. W. & Radewan, C. H. (1977). Kalman filtering in two dimensions. *IEEE Transactions on Information Theory*, 23, pp. 473–482.
- Zheng, D.; Rademacher, J.; Chen, J.; Crow, T.; Bresee, M.; Moine, J.L. & Ryu, R. (2004). Estimating aboveground biomass using Landsat 7 ETM+ data across a managed landscape in northern Wisconsin, USA, *Remote Sensing of Environment*, 93, pp. 402–411.

IntechOpen

IntechOpen



## **Biomass - Detection, Production and Usage**

Edited by Dr. Darko Matovic

ISBN 978-953-307-492-4

Hard cover, 496 pages

**Publisher** InTech

**Published online** 09, September, 2011

**Published in print edition** September, 2011

Biomass has been an intimate companion of humans from the dawn of civilization to the present. Its use as food, energy source, body cover and as construction material established the key areas of biomass usage that extend to this day. Given the complexities of biomass as a source of multiple end products, this volume sheds new light to the whole spectrum of biomass related topics by highlighting the new and reviewing the existing methods of its detection, production and usage. We hope that the readers will find valuable information and exciting new material in its chapters.

### **How to reference**

In order to correctly reference this scholarly work, feel free to copy and paste the following:

Jalal Amini and Josaphat Tetuko Sri Sumantyo (2011). SAR and Optical Images for Forest Biomass Estimation, Biomass - Detection, Production and Usage, Dr. Darko Matovic (Ed.), ISBN: 978-953-307-492-4, InTech, Available from: <http://www.intechopen.com/books/biomass-detection-production-and-usage/sar-and-optical-images-for-forest-biomass-estimation>

**INTECH**  
open science | open minds

### **InTech Europe**

University Campus STeP Ri  
Slavka Krautzeka 83/A  
51000 Rijeka, Croatia  
Phone: +385 (51) 770 447  
Fax: +385 (51) 686 166  
[www.intechopen.com](http://www.intechopen.com)

### **InTech China**

Unit 405, Office Block, Hotel Equatorial Shanghai  
No.65, Yan An Road (West), Shanghai, 200040, China  
中国上海市延安西路65号上海国际贵都大饭店办公楼405单元  
Phone: +86-21-62489820  
Fax: +86-21-62489821

© 2011 The Author(s). Licensee IntechOpen. This chapter is distributed under the terms of the [Creative Commons Attribution-NonCommercial-ShareAlike-3.0 License](#), which permits use, distribution and reproduction for non-commercial purposes, provided the original is properly cited and derivative works building on this content are distributed under the same license.

IntechOpen

IntechOpen